Label-free imaging of cellular organization in living mammalian cells via external apodization phase-contrast microscopy

Lay Nurhana Sari[1], Takafumi Miyamoto[*1,2], Takenori Nishimura[3], Kenta Kainoh[1], Naoko Onodera[1], Mayuko Kano[1], Masato Masuda[4], Yoshiaki Tamura[4], Yusuke Hayashi[5], Yusuke Yamamoto[5], Shin-Ichiro Takahashi[3], Yuta Mishima[2,6], Yosuke Yoneyama[7], Yoshinori Takeuchi[1], Hiroshi Ohno[1], Yoshitaka Ohashi[1], Motohiro Sekiya[1], Takashi Matsuzaka[1,2], Hitoshi Shimano[*1]

1. Department of Endocrinology and Metabolism, Institute of Medicine, University of Tsukuba, Tsukuba, Ibaraki 305-8575, Japan.
2. Transborder Medical Research Center, University of Tsukuba, Tsukuba, Ibaraki 305-8577, Japan.
3. Department of Animal Sciences and Applied Biological Chemistry, Graduate School of Agricultural and Life Sciences, The University of Tokyo, Tokyo 113-8654, Japan.
4. Department of Information Sciences and Arts, Faculty of Information Sciences and Arts, Toyo University, Saitama 350-8585, Japan.
5. Laboratory of Integrative Oncology, National Cancer Center Research Institute, Tokyo 104-0045, Japan.
6. Department of Clinical Medicine, Institute of Medicine, University of Tsukuba, Tsukuba, Ibaraki 305-8575, Japan.
7. Institute of Research, Tokyo Medical and Dental University, 1-5-45, Yushima, Bunkyo-ku, Tokyo 113-8510, Japan.

*Correspondence to: takmi565@md.tsukuba.ac.jp, hshimano@md.tsukuba.ac.jp

Abstract

Developing techniques to visualize the dynamics of cellular organization, which impacts the spatiotemporal functionality of biomolecules, is essential for elucidating mechanisms that govern cellular behavior. In this study, we demonstrated that label-free external apodization phase-contrast (ExAPC) microscopy is a valuable modality for this purpose, as this method can be used to visualize refractive index changes in intracellular structures, achieves high spatiotemporal resolution and suppresses halos. Utilizing the ability of ExAPC microscopy to visualize various intracellular structures simultaneously, we successfully captured detailed alterations in cellular organization during diverse cellular behaviors. Furthermore, through quantitatively analyzing the images obtained by combining ExAPC microscopy with fluorescence microscopy, we discovered characteristic heterogeneities in biomolecular condensates, lipid droplets, and mitochondria. This study underscores the potential of ExAPC microscopy for providing detailed images of alterations in cellular organization associated with various cellular behaviors, thereby corroborating the existing knowledge and potentially revealing novel discoveries.

Introduction

Cells harbor intracellular compartments called organelles that perform many diverse functions. The characteristic dimensions, quantities, and spatial arrangements of each organelle lead to the overall morphological attributes of the cell, termed cellular organization[1]. Many researchers have suggested that cellular organization, in concert with the functional attributes of cellular organelles, plays a pivotal role in determining diverse cellular behaviors[2-5].

To gain insight into the significance of cellular organization and its critical roles in various cellular behaviors, it is imperative to visualize and clarify the intricate nature of cellular organization. Fluorescence imaging has emerged as an irreplaceable tool for achieving this goal[6,7]. This imaging modality employs fluorescent moieties that selectively associate with target molecules, enabling meticulous and comprehensive visual representation of cellular organization. Due to continuous advancements in molecular genetic tools, fluorescent labeling has become increasingly accessible and exhibits several advantages, including swiftness, specificity, and broad applicability across diverse model organisms. However, fluorescence imaging has certain limitations, including photobleaching and phototoxicity[8]. Therefore, in recent decades, label-free imaging, which visualizes cells with minimal interference by exploiting the optical contrast caused by interactions between light and cells, has garnered interest from researchers[9]. This methodology does not involve labor-intensive labeling procedures and can generate images of samples in a closer-to-native state.

Several captivating label-free imaging techniques have been devised[10-12], among them being external apodization phase-contrast (ExAPC) microscopy[13]. In the ExAPC microscopy technique, a sample of interest is positioned in the front focal plane of the objective lens and is illuminated by light, which passes through an annular aperture. Due to partial diffraction, a portion of the incident light passes through an apodized phase plate, inducing a phase shift. The apodized plate ring employed in this technique is unique because two light-attenuating rings enclosing the phase ring are incorporated, which differs from conventional designs. The diffracted light that passes through these rings is effectively attenuated, reducing the contribution of diffracted rays to the generation of halo artifacts[14]. In addition, the apodized phase plate ring is placed externally, allowing the use of state-of-the-art objective lenses to produce high-resolution images (Fig. 1a). Accordingly, the multiplexing capability of phase-contrast microscopy, through which multiple cellular organelles can be imaged simultaneously, is utilized to generate high-resolution images, thereby facilitating the imaging and quantitative analysis of cellular organization dynamics. However, the utility of ExAPC microscopy as a label-free imaging technique has yet to be validated.

Here, we elucidate the cellular structures that can be identified by ExAPC microscopy and substantiate the efficacy of ExAPC microscopy in the detailed examination of biomolecular condensates, lipid droplets, and mitochondria. Utilizing the distinctive capabilities of ExAPC microscopy enables us to gain profound insights into the dynamics of intracellular structures and their consequential impacts on cellular behavior.

Results

Visualization of cellular organization in living cells at high resolution using ExAPC microscopy

Through ExAPC microscopy, diverse intracellular structures in living cells can be visualized. However, accurately discriminating a wide range of intracellular structures in cells solely based on these images is challenging (Fig. 1b). Therefore, we investigated whether specific organelles possess identifiable refractive index characteristics. The results showed that the nucleus, nucleolus, and mitochondria, but not the entire endoplasmic reticulum or Golgi apparatus, were clearly visualized by ExAPC microscopy, similar to conventional label-free techniques (Fig. 1c)[10,15].

We also discovered that certain vesicles that measured approximately 0.177 ± 0.168 μm^2 (n = 1,239), hereby referred to as endosome-like structures, corresponded to lysosomes (Fig. 1c). Additionally, actin filaments, but not microtubules, were observable by ExAPC microscopy (Fig. 1c). Observation of intracellular structures via ExAPC microscopy was also confirmed to be feasible in other live cell lines (Supplementary Fig. 1).

Obtaining reliable information on the dynamics of cellular organization provides insight into the mechanisms underlying various cellular behaviors. ExAPC microscopy leverages the apodization method to remove halos effectively[13]. Accordingly, ExAPC microscopy allowed us to discern intricate details associated with alterations in cellular organization during the division of HeLa cells and human induced pluripotent stem cells (hiPSCs) (Fig. 2a and Supplementary Movies 1, 2). We also successfully captured the changes in cellular organization during apoptosis (Fig. 2b and Supplementary Movie 3) and the process of target cell engulfment through entosis, except for areas obscured by the halo (Fig. 2c and Supplementary Movie 4). Imaging with an ExAPC microscope was a stable process and enabled long-term observation of the above cellular behaviors (Fig. 2). These results indicate that ExAPC microscopy facilitates spatial and temporal observation of cellular organization in living cells, as specific intracellular structures and their behaviors can be simultaneously captured while suppressing halos.

ExAPC microscopy-based analysis of biomolecular condensates and their analogous structures

Fluorescence microscopy delineates cellular organization using intracellular structure-specific fluorescent markers. In contrast, ExAPC microscopy transmutes the phase shift instigated by light that traverses the cellular entity into a shift in amplitude, which generates a variation in image contrast. Consequently, unlike fluorescence imaging modalities, ExAPC microscopy simultaneously visualizes the arrangement of all intracellular structures that cause phase shifts within the cell without staining.

When utilizing ExAPC microscopy to examine the cellular organization of living HeLa cells, we observed dynamic and distinct contrasting spherical structures in the cytoplasm that were absent in the organelles shown in Figure 1 (Fig. 3a and Supplementary Movie 5). This structure was perceptible in 16.3% (45 out of 276 cells) of the HeLa cells. A similar structure was also observed in the hiPSCs (Supplementary Movie 2). There was a weak correlation between the area and average intensity of BCLs observed in HeLa cells (Fig. 3b). Through time-lapse imaging, we ascertained that these structures exhibited fusion events (Fig. 3c), and treating cells with 1,6-hexanediol (1,6-HD), a known agent for dissolving liquid–liquid phase separated biomolecular condensates[16], resulted in their disappearance (Fig. 3d). Furthermore, subjecting HeLa cells to hyperosmotic stress, a known inducer of biomolecular condensate formation[17], led to the emergence of similar structures in the cytosol (Fig. 3e). Based on these results, we designated these structures biomolecular condensate-like structures (BCLs). The BCLs exhibited dynamic alterations in perimeter (Fig. 3f) and localization (Fig. 3g) in comparison to those of nucleoli, the major biomolecule that condenses in the nucleus[18]. Thus, the mechanisms governing the structural stability and localization of BCLs may differ from those of the nucleolus.

To further confirm the ability of ExAPC microscopy in observing biomolecular condensates, we focused on insulin receptor substrate 1 (IRS-1). IRS-1 is a crucial protein responsible for modulating insulin/insulin-like growth factor (IGF) signaling[19-21], and it has recently been determined that phase separation of IRS-1 promotes the formation of insulin/IGF signalosomes (termed the IRS-1 droplet)[22]. Upon exogenous expression of green fluorescent protein (GFP)-fused IRS-1 in U-2 OS cells, we observed the formation of IRS-1 droplet, as previously reported[22], by epifluorescence imaging and ExAPC imaging (Fig. 3h and Supplementary Fig. 2a). Additionally, through ExAPC microscopy, we observed fusion between IRS-1 droplets at various intracellular

locations (Fig. 3i and Supplementary Movie 6). Notably, 23.5% (167 out of 712) of the IRS-1 droplets were discernible via epifluorescence imaging, whereas no corresponding structures were evident in the ExAPC images (Supplementary Fig. 2b). Although the IRS-1 droplets were not significantly different in size from those that were visible and those that were invisible by ExAPC imaging, the fluorescence intensity of the IRS-1 droplets not visible by ExAPC imaging was significantly lower (Supplementary Fig. 2c, d). Nevertheless, determining the visibility of IRS-1 droplets by ExAPC imaging based solely on fluorescence intensity was challenging (Supplementary Fig. 2e). The variability observed in the visibility of the IRS-1 droplets through ExAPC microscopy could be attributed to the lower refractive indices of these IRS-1 droplets compared to others (Supplementary Fig. 2f, IRS-1 droplet #1) and to the presence of intracellular structures with nearly identical refractive indices (Supplementary Fig. 2f, IRS-1 droplet #2).

We then focused on IRS-1 droplets that were observable via both fluorescence and ExAPC microscopy. The size of the IRS-1 droplet was determined to be 0.76 ± 1.90 μm^2 by epifluorescence imaging and 0.77 ± 1.82 μm^2 by ExAPC imaging, with a strong correlation between the two (Fig. 3j). Conversely, the intensity of the IRS-1 droplet in the epifluorescence imaging weakly correlated with that in the ExAPC imaging (Fig. 3k). Time-lapse imaging revealed that the perimeter and localization of IRS-1 droplets, like those of BCLs, varied dynamically (Fig. 3l, m). Furthermore, we leveraged the multiplexing capability of ExAPC microscopy to investigate the organelles that interact with IRS-1 droplets. Consistent with the findings of a previous study[23], we observed that IRS-1 droplets contact nuclei, mitochondria, and endosome-like structures (Fig. 3n). Notably, contacts with endosome-like structures were observed at a high frequency, some of which lasted less than 1 second (Fig. 3o). Thus, it is conceivable that IRS-1 droplets may efficiently modulate the signal transduction performed by IRS-1 on other organelle membranes by selectively accumulating IRS-1 into specific intracellular compartments.

Dissection of lipid droplet formation using ExAPC microscopy

Lipid droplets (LDs) are prominent intracellular structures that are readily discernible through label-free imaging. These LDs begin to form as neutral lipids deposit between the leaflets of the endoplasmic reticulum bilayer[24,25], and their growth is orchestrated by de novo synthesis of triacylglycerols (TAGs) on the LD membranes and through fusion events among LDs[26,27]. We obtained time-lapse images of HeLa cells with 200 μM oleic acid to observe the biosynthesis of LDs in detail using ExAPC microscopy (Supplementary Fig. 3a). Of the structures observed by ExAPC microscopy, those stained with Lipi-Blue, which enhances fluorescence in a hydrophobic environment[28], were designated LDs (Supplementary Fig. 3b). Consequently, the entire trajectory, commencing from the initial appearance to the subsequent growth of LDs, was meticulously confirmed via ExAPC microscopy (Fig. 4a and Supplementary Movie 7). When the LD diameter was less than 450.4 ± 70.9 nm, it was observed as a white or black dot-like structure (Supplementary Fig. 3c, d). On the other hand, when the LD diameter exceeded the size, the appearance of the LD changed from the dot-like structure to a ring-like structure (Supplementary Fig. 3e, f). Notably, the images of the ring-like LDs varied depending on the focal position (Supplementary Fig. 3f). We defined phase 0 as the period when no LDs were observed, followed by phases 1 to 3, depending on the diameter of the LDs (Fig. 4a).

After the 218 LDs that were Lipi-Blue positive in the last frame were analyzed, 176 LDs appeared as phase 1 LDs during time-lapse imaging, and the mean diameter of the LDs was 285.6 ± 66.2 nm (Fig. 4b). This diameter is close to the size of pre-LDs (257.6 ± 31 nm), a restricted ER microdomain with a stable core of neutral lipids in the early stages of LD biogenesis[29]. The size of the LDs when they appeared in phase 1 remained constant over time following the addition of oleic acid (Fig. 4b). We next measured the time needed for each LD to reach each phase. As a

result, the transitions to phase 1, 2, and 3 were observed at 143.3 ± 116.4 min (n = 176), 161.9 ± 92.1 min (n = 162), and 239.6 ± 76.4 min (n = 123), respectively, after image acquisition began (Supplementary Fig. 3g). The mean time to reach each phase differed significantly among the cells (Supplementary Fig. 3g). Furthermore, the growth of each LD was heterogeneous after oleic acid was added (Fig. 4c). We also determined that the growth rate of LDs from phase 2 to phase 3 was 110.3 ± 44.0 min (n = 101), indicating that the average growth rate of LDs was 0.012 ± 0.004 × 10^{-3} μm^3/sec (Fig. 4d). The growth rate of each LD differed significantly among cells (Fig. 4d). Of note, there was no change in LD size due to fusion or division of LDs during the period we observed.

LDs frequently engage in various interactions with organelles, serving as sources of lipids for energy production and signal transduction[30]. Using ExAPC microscopy, we successfully observed the interactions between LDs and various organelles, such as mitochondria and the nucleus, in a label-free manner (Fig. 4e). Furthermore, upon tracking the dynamics of LDs, we discovered that these LDs do not remain stationary within the same location but migrate to certain subcellular compartments (Fig. 4f, g). The migration velocity of LDs was determined to be 0.01 ± 0.006 μm/sec (Fig. 4h), and a statistically significant variation was observed across different cells (Fig. 4i). Collectively, these findings imply the presence of cellular mechanisms that govern the subcellular localization and migration velocity of LDs.

Mitochondrial dynamics analyzed by ExAPC microscopy

Mitochondria are dynamic organelles that undergo highly regulated fission and fusion events[31]. Disruption of these regulatory mechanisms has been implicated in the development of various diseases, including cancer, cardiovascular disease, and neurodegenerative disorders[32]. Therefore, observing mitochondrial morphology is critical for clarifying pathological phenomena. However, assessing mitochondrial morphology with fluorescence imaging requires proper mitochondria-specific probes and imaging parameters, such as light intensity and exposure time[33]. In contrast, through ExAPC microscopy, mitochondrial morphology can be unambiguously visualized in a label-free manner; thus, compared to fluorescence imaging, ExAPC microscopy is more convenient and facilitates more detailed longitudinal observations.

We exploited the capabilities of ExAPC microscopy to investigate spontaneous mitochondrial fission and fusion processes devoid of pharmacological or genetic induction. Consequently, we accurately delineated the locations of fission in mitochondria with diverse shapes and lengths, similar to observations attained via fluorescence imaging[34] (Fig. 5a). Mitochondrial fission is induced when the ER and dynamin-related protein 1 (DRP1) cooperatively constrict mitochondrial cleavage sites[35,36]. We observed this constriction at mitochondrial cleavage sites via ExAPC microscopy (Fig. 5b and Supplementary Movie 8). Fission sites were distributed across the relative length of the mitochondria, showing a gradual bimodal distribution (Fig. 5c). These results support the presence of two distinguishable types of mitochondrial fission mechanisms, as previously evidenced[34]. We further examined whether mitochondrial length affects mitotic position but found no significant correlation between the mitochondrial length and fission site (Fig. 5d).

The mitochondrial fusion process was then meticulously observed (Fig. 5e, h). Mitochondrial fusion is a two-step process, in which mitofusins (MFNs) regulate outer mitochondrial membrane fusion and optic atrophy-1 (OPA1) governs inner mitochondrial membrane fusion in mammalian cells[37]. Typically, mitochondrial fusion occurs at the ends of both mitochondria, although end-to-side fusion occurs in rare instances, as previously reported[38] (Fig. 5f and Supplementary Movie 9, 10). As was confirmed for mitochondrial fission, a gradual bimodal distribution was also observed for the relative lengths of the two fusing mitochondria (Fig. 5g).

However, the relative length of the smaller of the two fused mitochondria was greater than 30% in 80.7% of the fusion events, indicating that mitochondria of similar length tend to fuse with each other (Fig. 5g). As with mitochondrial fission events, we found no substantial correlation between mitochondrial length and fusion location (Fig. 5h). These results suggest that the ratio of individual mitochondrial lengths involved in these events should be considered when examining the complex processes governing mitochondrial fission and fusion.

Administering an uncoupler of oxidative phosphorylation, such as carbonylcyanide-p-trifluoromethoxyphenylhydrazone (FCCP), leads to a reduction in mitochondrial membrane potential (ΔΨm) and induces reactive oxygen species (ROS) stress within the cell; these processes cause the mitochondrial structures to transform from elongated string-like structures to small globular structures that are scattered throughout the cell[39]. However, the characteristics in mitochondrial morphology that follow ΔΨm loss remain controversial. To address this topic, we employed ExAPC microscopy and examined the rapid alterations in mitochondrial morphology upon FCCP treatment. Treatment with 40 μM FCCP precipitously diminished the ΔΨm (Fig. 5i and Supplementary Fig. 4a). Consequently, the morphology of individual mitochondria in Hep3B cells transitioned from string-like structures to globular structures within seconds (Fig. 5j and Supplementary Movie 11). In contrast, in U-2 OS cells, only a portion of the mitochondrion exhibited spherical morphologies (Supplementary Fig. 4b and Supplementary Movie 12). Furthermore, the process of mitochondrial morphology change upon FCCP treatment was different in individual mitochondria in both Hep3B and U-2 OS cells (Fig. 5j and Supplementary Fig. 4b). These results suggest that there is heterogeneity in the responsiveness of mitochondria to FCCP.

Mitochondria are recognized for their ability to communicate through contacting each other[40]. We observed this communication between mitochondria by ExAPC microscopy under normal culture conditions as well as conditions in which the ΔΨm was disrupted by FCCP treatment (Fig. 5k, l). These results indicate that intermitochondrial communication does not necessarily require the ΔΨm.

Discussion

In this study, we showed that ExAPC microscopy is a highly suitable tool for examining cellular organization and organelles. With its exceptional spatiotemporal resolution and multiplexing capabilities, this label-free imaging modality facilitates the simultaneous visualization of numerous intracellular structures and allows detailed scrutiny of morphological changes within cellular organization across the spectrum of physiological and pathological phenomena. Despite the recent emergence of photostable fluorescent proteins[41,42], it is worth emphasizing that label-free imaging exhibits distinct advantages, as prolonged observations of living cells can be achieved with minimal phototoxicity concerns and negligible photobleaching.

Biomolecular condensates are membrane-free intracellular compartments that may play a pivotal role in orchestrating complex and diverse biochemical reactions with spatial and temporal precision[43,44]. Nevertheless, several critical uncertainties remain, including the processes that govern the genesis of biomolecular condensates and the resultant modifications in the functionality of biomolecules sequestered in these entities. Here, via ExAPC microscopy, we discovered the presence of BCLs, the exact composition of which remains elusive. Further studies are needed, but we anticipate that the observation of BCLs using ExAPC microscopy will contribute to a more comprehensive understanding of biomolecular condensates. Notably, when observing IRS-1 droplets under the ExAPC microscope, we identified IRS-1 droplets that lack distinguishable refractive indices from their surroundings. This observation suggests the presence of IRS-1 droplets with differing compositions. In the last decade, researchers have

attempted to elucidate the function of biomolecular condensates in diseases such as neurodegeneration and cancer[45-47]. In addition to the accumulated knowledge to date, it may be crucial to consider the heterogeneity of biomolecular condensates in the future.

Intracellular LDs are conserved organelles found in all eukaryotic cells[48]. They serve as repositories for lipids, including TAGs and sterol esters, and play a vital role in safeguarding cells from lipotoxicity by sequestering fatty acids[49]. LDs can form when TAGs accumulate within the lipid bilayer of the endoplasmic reticulum and subsequently bud into the cytosol. These nascent LDs can grow through fusion events or de novo synthesis of TAGs on their surfaces. In the case of fusion, it is well established that neutral lipids are transported from smaller to larger lipid droplets through channel-like associations, which is mediated by the lipid droplet-associated protein FSP27, as well as perilipin1[50]. However, while FSP27 is expressed in numerous tissues, perilipin1 is found primarily in testicular, breast, and adipose tissues and is rarely expressed in HeLa cells[51,52]. Accordingly, our study revealed the presence of adjacent LDs for a certain duration; however, no fusion events between these lipid droplets were detected. In contrast, the latter mechanism involves the transfer of TAG synthesis-related enzymes localized within the endoplasmic reticulum to the LD membrane via membrane-to-membrane connections, and subsequently, the TAGs synthesized on the membrane are added to the lipid droplet core[26]. HeLa cells harbor TAG synthesis-related enzymes, such as glycerol-3-phosphate acyltransferase (GPAT), 1-acylglycerol-3-phosphate O-acyltransferase 1 (AGPAT), lipin/phosphatidic acid phosphatase (PAP), and diacylglycerol acyltransferase (DGAT)[51]. This finding supports the notion that the latter mechanism primarily underlies the oleic acid-induced formation of LD in HeLa cells.

Early LDs are known for their short life span and diminutive size, which often poses challenges in their visualization[49]. Previous research has indicated that the diameter of nascent lipid droplets varies, ranging from 30 to 60 nm in yeast studies that involved electron microscopy[25] to ~170 nm in mammalian cell lines[53]. Notably, examination of the nascent process of LDs through ExAPC microscopy revealed an initial LD size of 280.7 ± 65.8 nm. Accordingly, ExAPC microscopy facilitates the observation of relatively early nascent lipid droplets. Furthermore, in our study, the growth rate of LDs was calculated to be $0.012 \pm 0.004 \times 10^{-3}$ μm^3/sec. This growth rate of LDs was closer to the rate observed in COS-1 cells (0.043×10^{-3} μm^3/sec)[29] than to the rate observed in Drosophila (0.159×10^{-3} μm^3/sec)[26]. Accumulating quantitative data and elucidating the constituents of individual LDs will enable us to calculate the kinetics of biochemical reactions involved in the growth of single lipid droplets; this information will facilitate additional in-depth investigations into lipid droplets.

Mitochondria are recognized as multifunctional organelles that undergo dynamic morphological changes through repeated fission and fusion processes[54]. Mitochondria exhibit a plethora of distinct morphologies within different cells, ranging from reticulated throughout the cell to fragmented into discrete pieces[55]. In recent decades, a series of distinctive morphological alterations in mitochondria have been reported during processes such as stem cell differentiation and in multifactorial diseases, such as cancer, cardiovascular diseases, and neurodegenerative diseases[5,56,57]. These observations underscore the importance of mitochondrial morphology as a factor in various physiological and pathological events. Hence, clarifying the regulatory mechanisms that govern mitochondrial fission and fusion is imperative, as these processes play pivotal roles in determining mitochondrial morphology. In this study, we observed a bimodal distribution of fission positions along the length of mitochondria. Conversely, during fusion events, mitochondria tend to fuse with other mitochondria of comparable length. The underlying mechanism for this selective preference remains elusive; however, mitochondria may possess the capacity to perceive neighboring mitochondria that exhibit analogous length characteristics. Furthermore, we revealed that $\Delta\Psi m$ loss leads to distinct morphological

changes; in Hep3B cells, the entire mitochondrion assumes a spherical morphology, whereas in U-2 OS cells, only a portion of the mitochondrion adopts this morphology. This discrepancy in changes in mitochondrial morphology between Hep3B and U-2 OS cells after ΔΨm loss may result from differences in the quantity and composition of mitochondrial lipids. Despite the universality of mitochondrial function across cells, questions remain as to how differences in mitochondrial morphology at steady state and in responsiveness to specific stimuli affect mitochondrial functions. We also observed that individual mitochondria respond differently to FCCP. This heterogeneity observed in the responsiveness of individual mitochondria within the same cell may be crucial for precisely regulating the responsiveness of mitochondria as a whole within the cell. Indeed, it has been reported that the presence of variability in cellular responses enables more accurate control of tissue responses, which are collections of cells[58]. Similar regulatory systems might also exist within mitochondria. Further investigations are needed to clarify these questions. We believe that ExAPC microscopic data will catalyze the exploration of these biological questions and contribute to a deeper understanding of life phenomena.

Owing to its label-free nature, ExAPC microscopy has facilitated detailed examination of how biomolecular condensates, LDs, and mitochondria engage in communication with various cellular organelles. We successfully observed communication between these intracellular structures without staining steps using ExAPC microscopy. On the other hand, it was difficult to completely reduce halos in cell specimens, even with the use of an apodized plate ring. To enable label-free imaging of cells without halos, other modalities, such as holo-tomographic microscopy[10], should be considered. The optimal microscopy modality is contingent upon the characteristics of a subject and the prioritization of temporal versus spatial resolution. Furthermore, to comprehend the underlying mechanisms of various cellular behaviors, it is essential not merely to observe cellular behaviors through a singular modality but rather to observe them through multiple modalities and comprehensively interpret the obtained information. In recent years, single-cell omics technologies have advanced significantly, with rapid progress in the development of foundational techniques to enable real-time omics analysis[59-61]. Integrating these technologies with label-free imaging techniques possessing multiplexing capabilities, such as ExAPC microscopy, is a key challenge in the future of imaging technologies.

Methods

Plasmid construction

EYFP-Cb5 was produced by subcloning the sequence coding aa 100–134 of rat Cytochrome b5 (UniprotKB-P00173) into an EYFP vector at the C-terminus between the EcoR I and Sal I sites. EYFP-sGOLGB1 was produced by subcloning the sequence encoding aa 3131–3259 of human GOLGB1 (UniProtKB-Q14789) into an EYFP vector at the C-terminus between the EcoR I and Sal I sites. Lifeact-EYFP was kindly provided by Dr. Hideki Nakamura (Kyoto University). GFP-rIRS-1 was produced by subcloning the sequence coding aa 4–1235 of rat IRS-1 (UniProtKB-P35570) into an EGFP vector at the C-terminus between Hind III and the BamH I site.

Cell culture and transfection

Human lung carcinoma A549 cells (CCL-185), human cervical adenocarcinoma HeLa cells (CCL-2), human colon carcinoma HCT116 cells (CCL-247), human hepatocellular carcinoma Hep 3B cells (HB-8064), mouse fibroblast NIH/3T3 cells (CRL-1658), human breast adenocarcinoma MDA-MD-231 cells (CRM-HTB-26), human osteosarcoma U2-OS cells (HTB-96), and human breast carcinoma ZR75-1-1 (CRL-1500) cells were purchased from the American Type Culture Collection. These cells, except ZR75-1-1, were cultured in Dulbecco's modified Eagle's medium (DMEM;

Thermo Fisher Scientific, 11965118) supplemented with 10% fetal bovine serum (FBS; Thermo Fisher Scientific, 10270-106) and 1% Zell Shield (Minerva Biolabs GmbH, 13-0050) at 37°C in 5% CO_2. ZR75-1-1 cells were cultured in RPMI 1640 medium (Thermo Fisher Scientific, 11875093) supplemented with 10% FBS and 1% Zell Shield at 37°C in 5% CO_2. For transient transfection, 2×10^5 cells were plated on a 35 mm imaging dish with a polymer coverslip bottom (ibidi, 80136) and incubated for 6 h at 37°C in 5% CO_2. Following incubation, the cells were transfected with the plasmid using FuGENE HD (Promega, E2311). The indicated experiments were carried out 12–18 h after transfection. The TKT3V1-7 iPSC clone was generated from peripheral blood T cells by Sendai virus reprogramming vectors as previously described[62]. The iPSC line was provided by CiRA with the approval of the Ethical Review Board of CiRA (no. G590). iPSCs were maintained on an iMatrix-511 (Matrixome, Japan) as previously described[63], but StemFit AK02N (Ajinomoto, Japan) was used instead of AK03.

Live-cell imaging

For ExAPC microscopy, a phase ring was inserted into an inverted Eclipse Ti2-E microscope (Nikon) to obtain images without phase-contrast objectives (the motorized external phase-contrast system, Nikon). Phase contrast images were obtained using an oil-immersion lens (CFI Apochromat TIRF 100XC Oil, NA = 1.49, Nikon). For epifluorescence microscopy images, BFP, EYFP, and mCherry excitation was carried out using an Intensilight mercury-fiber illuminator (Nikon). The data were processed through a BFP-A-Basic filter (Semrock), a CFP-A-Basic-NTE filter (Semrock), a YFP-A-Basic-NTE filter (Semrock), and an mCherry-B-NTE-ZERO filter (Semrock) for BFP, EYFP, and mCherry imaging, respectively. The cells were viewed using a 100× objective mounted on an inverted Eclipse Ti2-E microscope (Nikon) and imaged using a Zyla 4.2 PLUS sCMOS camera (Oxford Instruments). Imaging data were processed using NIS-Elements AR imaging software (Nikon).

All imaging experiments were completed at 37°C in 5% CO_2 using an STX stage top incubator (Tokai-Hit). For all live-cell imaging, unless otherwise noted, cells were cultured in phenol red-free DMEM (Thermo Fisher Scientific, 31053028) supplemented with 10% FBS, 4 mM L-glutamine (Thermo Fisher Scientific, 25030081), and 1% penicillin–streptomycin (Sigma–Aldrich, P4333). The following representative images obtained by epifluorescence microscopy were processed by Clarify.ai and Denoise.ai using NIS-Elements AR 5.30: mitochondria, ER, Golgi apparatus, and lysosome.

Organelle staining

A total of 2×10^5 cells were plated on a 35 mm imaging dish with a polymer coverslip bottom and incubated for 12–18 h at 37°C in 5% CO_2. Following incubation, the cells were cultured with 0.1 μg/ml Hoechst 33342 (Thermo Fisher Scientific, 62249) for 10 min at 37°C in 5% CO_2 to stain the nuclei. For mitochondrial staining, the cells were cultured with 0.5 μM MitoTracker Red CM-H2Xros (Thermo Fisher Scientific, M7513) for 30 min at 37°C in 5% CO_2. For lysosome staining, the cells were cultured with 100 nM LysoTracker Red DND-99 (Thermo Fisher Scientific, L7528) for 30 min at 37°C in 5% CO_2. For tubulin staining, the cells were cultured with 1.3 ng/μl Tubulin Tracker™ Green (Thermo Fisher Scientific, T34075) for 30 min at 37°C in 5% CO_2. The cells were then washed with imaging medium twice and subjected to live-cell imaging.

Monitoring cell division

For the HeLa cells, 2×10^5 cells were plated on a 35 mm imaging dish with a polymer coverslip bottom and incubated for 24 h at 37°C in 5% CO_2. For iPSCs, 1.3×10^5 cells were plated on a 35 mm imaging dish with a polymer coverslip bottom at 37°C in 5% CO_2. After 72 h, live-cell imaging

was carried out with the iPSC culture medium.

Monitoring of apoptosis

HeLa cells (2×10^5 cells) were plated on a 35 mm imaging dish with a polymer coverslip bottom and incubated for 24 h at 37°C in 5% CO_2. Subsequently, the cells were subjected to live-cell imaging. Then, 1 μM staurosporine (Sigma–Aldrich, S6942-200UL) was added at the indicated times.

Monitoring entosis

ZR75-1-1 cells (4×10^5 cells) were seeded in three 6 cm dishes. Forty-eight hours later, 4 μl of 1 mM CellTracker Green CMFDA Dye (Thermo Fisher Scientific, C7025) was added to one dish and incubated for 30 min at 37°C in 5% CO_2. After incubation, the cells were washed 3 times with 4 ml of PBS. The ratio of stained cells to unstained cells was adjusted to 1:2, and these cells were plated onto 35mm imaging dishes with polymer coverslips (4×10^5 cells/dish) and incubated for 48 h at 37°C in 5% CO_2. Subsequently, the cells were subjected to live-cell imaging.

Monitoring BCLs and IRS-1 droplets

HeLa cells (2×10^5 cells) were plated on a 35 mm imaging dish with a polymer coverslip bottom and incubated for 24 h at 37°C in 5% CO_2. Subsequently, the cells were subjected to live-cell imaging. 1,6-Hexanediol (Sigma–Aldrich, 240117) and sodium chloride (Nacalai, 31320-05) were added at the indicated times. The perimeter, intensity, and motility of the BCLs and IRS-1 droplets were analyzed by NIS software (Nikon).

LD tracking and analysis

HeLa cells (2×10^5 cells) were plated on a 35 mm imaging dish with a polymer coverslip bottom and incubated for 24 h at 37°C in 5% CO_2. The cells were stained with 0.5 μM Lipi-Blue for 30 min according to the manufacturer's protocol. Oleic acid (200 mM; Sigma–Aldrich, O1008) was then added to the cells 20 min before live-cell imaging began. LD tracking was performed using NIS software (Nikon). For the classification of LDs from Phase 1 to Phase 3, LDs with diameters ranging from 0.51 to 0.64 μm were classified as Phase 2, while LDs smaller than this range were categorized as Phase 1, and those larger than this range were categorized as Phase 3. In calculating the growth rate of LDs from Phase 2 to Phase 3, only LDs that exhibited a transition from Phase 1 to Phase 3 during time-lapse imaging were included in the calculation. Heatmap cluster analysis was performed by Origin Pro 2023. For plotting the behavior of LDs, the coordinates of the nucleolus in the same cell were subtracted from the coordinates of the LD.

ΔΨm analysis

The cells were cultured for 30 min in the presence of 100 nM Image-iT TMRM Reagent (TMRM; Thermo Fisher Scientific, I34361) at 37°C in 5% CO_2. The cells were then washed with imaging medium twice, and TMRE fluorescence in the mitochondria was recorded with NIS software (Nikon). Background fluorescence was measured in areas without mitochondria and subtracted from the fluorescence obtained from mitochondria.

Statistical analysis

The results are presented as the means ± standard deviation. All the statistical tests were performed using GraphPad Prism (GraphPad Software) or Excel (Microsoft Office). The number of classes in the histogram is determined by the Sturgess formula.

Acknowledgments
We thank Katsuko Okubo (University of Tsukuba) for her technical assistance and Yasuko Maruyama (University of Tsukuba) for her generous support. We would like to thank Nature Research Editing Service for English language editing. This study was supported in part by a JSPS KAKENHI (22H02296), the Takeda Science Foundation (DGM06005J), JST COI-NEXT (JPMJPF2017), and JST CREST (JPMJCR1927).

Author contributions
T.Miyamoto. conceived the project. T.Miyamoto. designed the experiments. T. Miyamoto., L.N.S., T.N., K.K., N.O., M.K., M.M., Y.Y., Y.H., Y.Y., SI. T., Y.M., Y.Y., Y.T., H.O., Y.O., M.S., T.M., H.S. conducted the experiments. T.Miyamoto. and L.N.S. wrote the manuscript.

Figure legends

Figure 1. Visualization of cellular organization utilizing ExAPC microscopy

(a) Schematic representation of the ExAPC microscope used in this study. (b) ExAPC microscopy images depicting live A549 cells. Scale bar: 10 μm, Scale bar in inset: 10 μm. (c) Comparison of organelle visualization and intensity profiles using ExAPC and epifluorescence microscopy with the indicated organelle markers. Nucleus: Hoechst 33342; endoplasmic reticulum (ER): EYFP-Cb5; Golgi apparatus: EYFP-sGOLGB1; mitochondria: MitoTracker Red CMXRos; lysosomes: LysoTracker Red DND-99; actin: Lifeact-EYFP; tubulin: Tubulin Tracker Green. The intensities obtained by ExAPC microscopy are shown as absolute values after subtracting 1 from the normalized value. Scale bar: 10 μm, Scale bar in inset: 1 μm.

Figure 2. Visualization of diverse cellular behaviors using ExAPC microscopy

Representative images of the indicated cellular behaviors acquired by ExAPC microscopy are shown. (a) Cell division of HeLa cells and human induced pluripotent stem cells (hiPSCs). Acquisition rate: 1 min/frame. Arrowhead: Biomolecular condensate-like structure; see Figure 3. (b) HeLa cells were treated with 1 μM staurosporine (STS) at frame 15. Acquisition rate: 5 min/frame. (c) Entosis of ZR75-1 cells. Acquisition rate: 1 min/frame. (d) ZR75-1 cells stained with CellTracker Green CMFDA and unstained ZR75-1 cells were cocultured. Acquisition rate: 1 min/frame. Scale bar: 10 μm. Time: h:mm:ss.ms.

Figure 3. Visualization of BCLs and IRS-1 droplets via ExAPC microscopy

(a) Z-stack imaging of BCL in HeLa cells. Z-Step: 0.097 μm. Scale bar: 10 μm; scale bar in inset: 1 μm. (b) Relationship between the area and average intensity of BCLs observed in HeLa cells. n = 104 from 45 cells. (c) Time-lapse imaging showing the fusion of the two BCLs in HeLa cells. Acquisition rate: 1 sec/frame. Scale bar: 1 μm. (d) BCL-positive HeLa cells were treated with 5% 1,6-HD at Frame 61. Acquisition rate: 1 sec/frame. Scale bar: 10 μm; scale bar in inset: 1 μm. (e) HeLa cells were treated with 100 mM NaCl at Frame 61. Acquisition rate: 1 sec/frame. Scale bar: 10 μm; scale bar in the inset: 1 μm. The BCLs indicated by orange arrowheads were fused with the BCL indicated by the blue arrowhead. (f) Heatmaps of the perimeter ratios of BCLs and nucleoli in HeLa cells. Each row represents a single BCL (n = 104) or the nucleolus (n = 48). (g) Random motions of BCLs and the nucleolus in HeLa cells. The plots show BCLs and nucleoli over 60 s, starting at the center. The analyzed BCLs and nucleolus are the same as that in Figure 3f. (h) Representative images of U-2 OS cells expressing GFP-IRS-1. Scale bar: 10 μm. (i) Time-lapse imaging showing the fusion of two IRS-1 droplets in U-2 OS cells expressing GFP-IRS-1. Acquisition rate: 1 min/frame. Scale bar: 1 μm. (j and k) Relationships between the area of IRS-1 droplets measured from ExAPC and epifluorescence images (j) and the mean intensity of IRS-1 droplets measured from ExAPC and epifluorescence images (k). n = 545 from 15 U-2 OS cells expressing GFP-IRS-1. (l) Heatmaps of the perimeter ratio of IRS-1 droplets to nucleoli in 9 GFP-IRS-1-expressing U-2 OS cells. Each row represents a single IRS-1 droplet (n = 122) or a nucleolus (n = 23). (m) Random motion of IRS-1 droplets and nucleoli in U-2 OS cells expressing GFP-IRS-1. The plots show IRS-1 droplets and nucleoli over 60 s, starting at the center. The analyzed BCLs and nucleolus are the same as that in Figure 3l. (n) Interaction of IRS-1 droplets with various organelles in GFP-IRS-1-expressing U-2 OS cells. Scale bar: 10 μm; scale bar in the inset: 1 μm. (o) Kymograph showing the interaction between the IRS-1 droplets and endosome-like structures (arrowhead). Scale bar: 1 μm. Time: h:mm:ss.ms.

Figure 4. Visualization of LD dynamics using ExAPC microscopy

(a) [left] Growth process of LDs. [right] Time-lapse imaging was started 20 min after adding 200 μM oleic acid to the HeLa cells. See Supplementary Figure 3a. The cells shown here are the same as in Supplementary Figure 3b. Green arrowhead: LD being tracked. Scale bar: 10 μm; scale bar in inset: 1 μm. (b) Diameters of LDs recognized as Phase 1 at each time point after image acquisition began (frame 1: 0 min). Acquisition rate: 20 sec/frame. means ± SD. Number of LDs at each period from left to right: 51, 21, 29, 15, 10, 14, 12, 24. One-way ANOVA for multiple comparisons between each period. N.S., no significant difference. Total: all analyzed LDs (n = 176). (c) Heatmap of phase transitions for each LD (n = 218). The cells analyzed (Cell#1-5) and in each phase (Phase 0-3) are color-coded according to the legend below. The dendrogram shows a hierarchical clustering based on the time at which the phase transition occurred for each LD. (d) LD growth rate based on the Phase 2-3 transition time. means ± SD. The numbers of LDs analyzed were as follows: Cell#1: n = 23; Cell#2: n = 35; Cell#3: n = 8; Cell#4: n = 35; Cell#5: n = 0 (N.A.); and Total: n = 101. One-way ANOVA for multiple comparisons was performed between each cell. (e) Interaction of LDs with various organelles in HeLa cells. Green arrowhead: LD. Yellow arrowhead: organelle interacting with the LD. Scale bar: 1 μm. (f) LD dynamics. The coordinates of LDs are corrected for the coordinates of nucleoli in the same cell. The time at which the coordinates of each LD were obtained after the addition of oleic acid is color coded according to the legend on the right. The number of LDs is plotted as follows: Cell#1: n = 36; Cell#2: n = 44; Cell#3: n = 44; Cell#4: n = 65; and Cell#5: n = 28. (g) Euclidean distance between the coordinates at which each LD was first identified and the coordinates at the end of time-lapse imaging. The number of plotted LDs is the same as that in Figure 4f. (h) LD migration velocity in each cell (Cell #1-5) and in all cells (total). means ± standard deviation. The analyzed LDs is the same as that in Figure 4f. One-way ANOVA for multiple comparisons was performed between each cell. *$P < 0.05$, ****$P < 0.0001$. (i) LD migration velocity in each cell (Cell#1-5) in each phase. means ± standard deviation. The analyzed LDs is the same as that in Figure 4f. The numbers of LDs analyzed were as follows: [Phase 1] Cell#1: n = 33, Cell#2: n = 42, Cell#3: n = 42, Cell#4: n = 43, Cell#5: n = 28, [Phase 2] Cell#1: n = 36, Cell#2: n = 44, Cell#3: n = 38, Cell#4: n = 58, Cell#5: n = 10, [Phase 3] Cell#1: n = 25, Cell#2: n = 37, Cell#3: n = 8, Cell#4: n = 53, Cell#5: n = 0. One-way ANOVA for multiple comparisons was performed between each cell in each phase. *$P < 0.05$, **$P < 0.01$, ***$P < 0.001$, ****$P < 0.0001$.

Figure 5. Visualization of mitochondrial dynamics using ExAPC microscopy

(a) Gallery image of mitochondria from a binarized ExAPC microscopy movie one frame before division. (b) Time-lapse imaging of mitochondrial fission in Hep3B cells. (c) [Left] Position of mitochondrial fission relative to total mitochondrial length (n = 54 fissions pooled from multiple datasets). [Right] Histogram of fission positions relative to the total mitochondrial length in the left figure. Width: 5.32. (d) Correlation between shorter daughter mitochondria length and the position of mitochondrial fission relative to total mitochondrial length. The analysis of mitochondria was identical to that in Figure 5c. (e) Gallery image of mitochondria from a binarized ExAPC microscopy movie one frame before fusion. (f) Time-lapse imaging of mitochondrial fusion in Hep3B cells. (g) [Left] Position of mitochondrial fusion relative to total mitochondrial length (n = 26 fusions pooled from multiple datasets). [Right] Histogram of fusion positions relative to the total mitochondrial length in the left figure. Width: 5.69. (h) Correlation between shorter daughter mitochondria length and the position of mitochondrial fusion relative to total mitochondrial length. The analysis of mitochondria was identical to that in Figure 5g. (i) Mitochondrial membrane potential in Hep3B cells. Representative images at each time point are shown. All the data are presented as the mean ± standard deviation. 0 μM FCCP: n = 14 cells. 40

μM FCCP: n = 49 cells. (j) FCCP treatment-induced changes in mitochondrial morphology in Hep3B cells. FCCP was added after image acquisition at frame 301 (1 frame/sec). Scale bar: (Before Time-lapse imaging): 10 μm, (Time-lapse imaging): 1 μm. (k) Intermitochondrial communication in the presence or absence of FCCP in Hep3B cells. Scale bar: 1 μm.

Supplementary Figure 1. Various cell lines visualized by ExAPC microscopy

Representative images of the indicated cell lines acquired by ExAPC microscopy are shown. Nucleus: Hoechst 33342; mitochondria: MitoTracker Red CMXRos. Scale bar: 10 μm, Scale bar in inset: 1 μm.

Supplementary Figure 2. Visibility of IRS-1 droplets via ExAPC microscopy

(a) Z-stack imaging of IRS-1 droplets in U-2 OS cells. GFP-IRS-1 was transiently expressed in U-2 OS cells. Z-Step: 0.048 μm. Scale bar: 10 μm, Scale bar in inset: 1 μm. (b) line-scan profiles of intensity in the merged inset is shown. The intensities obtained by ExAPC microscopy are shown as absolute values after subtracting 1 from the normalized value. Scale bar: 10 μm; scale bar in inset: 1 μm. (c and d) Mean fluorescence intensity (c) and area (d) of IRS-1 droplets that cannot be detected in GFP-IRS-1-expressing U-2 OS cells via ExAPC microscopy. p: Unpaired t-tests. N.S., statistically nonsignificant. (e) Relationship between the IRS-1 droplet area and the mean intensity of IRS-1 in U-2 OS cells expressing GFP-IRS-1, as measured in Supplementary Figure 2c and 2d. (f) Z-stack image of an IRS-1 droplet that cannot be detected in U-2 OS cells via ExAPC microscopy. GFP-IRS-1 was transiently expressed in U-2 OS cells. Z-Step: 0.048 μm. Scale bar: 10 μm, Scale bar in inset: 1 μm.

Supplementary Figure 3. Visibility of LDs using ExAPC microscopy

(a) Schematic diagram of this experiment. (b) Oleic acid treatment-induced LD formation. HeLa cells were treated with oleic acid as described in supplementary figure 3a. The cells shown here are the same as in Figure 4a. Scale bar: 10 μm; scale bar in inset: 1 μm. (c) Representative images of LDs in Phase 1. Scale bar: 1 μm. (d) Diameter at the point of change in appearance from dot-like to ring-like LDs (n = 165). (e) Representative images of LDs in Phases 2 and 3 in oleic acid-treated HeLa cells. (f) The visibility of LDs according to the difference in focal planes. Scale bar: 1 μm. (g) Time for each LD to reach each phase defined by diameter. Mean ± standard deviation. [Total] Phase 1: n = 176, Phase 2: n = 162, Phase 3: 123, [Phase 1] Cell#1: n = 27, Cell#2: n = 36, Cell#3: n = 42, Cell#4: n = 42, Cell#5: n = 29, [Phase 2] Cell#1: n = 33, Cell#2: n = 42, Cell#3: n = 36, Cell#4: n = 42, Cell#5: n = 9, [Phase 3] Cell#1: n = 25, Cell#2: n = 37, Cell#3: n = 8, Cell#4: n = 53, Cell#5: n = 0. One-way ANOVA for multiple comparisons was performed between phases (total) and between cells (phases 1-3).

Supplementary Figure 4. Mitochondrial dynamics in the presence of FCCP in U-2 OS cells

(a) Mitochondrial membrane potential in U-2 OS cells. Representative images at each time point are shown. All the data are presented as the mean ± standard deviation. 0 μM FCCP: n = 9 cells. 40 μM FCCP: n = 32 cells. (j) FCCP treatment-induced changes in mitochondrial morphology in U-2 OS cells. FCCP was added after image acquisition at frame 301 (1 frame/sec). Green arrowhead: Mitochondrion with morphological changes. Scale bar: (Before Time-lapse imaging): 10 μm, (Time-lapse imaging): 1 μm.

Supplementary Movie 1. Cell division (HeLa cells)

HeLa cells were imaged by time-lapse ExAPC microscopy to visualize cell division. Images

acquired every 1 minute, movie presented at 10 frames per second. Scale bar: 10 μm. (MOV 53,770 kb)

Supplementary Movie 2. Cell division (iPSCs)
iPSCs were imaged by time-lapse ExAPC microscopy to visualize cell division. Images acquired every 1 minute, movie presented at 10 frames per second. Scale bar: 10 μm. (MOV 250,771 kb)

Supplementary Movie 3. Apoptosis
HeLa cells were imaged by time-lapse ExAPC microscopy to visualize apoptosis. HeLa cells were treated with 1 μM STS at frame 15. Images acquired every 5 minutes, movie presented at 10 frames per second. Scale bar: 10 μm. (MOV 22,362 kb)

Supplementary Movie 4. Entosis
ZR75-1 cells were imaged by time-lapse ExAPC microscopy to visualize entosis. Images acquired every 1 minute, movie presented at 10 frames per second. Scale bar: 10 μm. (MOV 131,018 kb)

Supplementary Movie 5. BCLs
HeLa cells were imaged by time-lapse ExAPC microscopy to visualize BCLs. Images acquired every 1 second, movie presented at 10 frames per second. Scale bar: 10 μm. (MOV 1,772 kb)

Supplementary Movie 6. IRS-1 droplet
U-2 OS cells expressing GFP-IRS1 were imaged by time-lapse ExAPC microscopy to visualize IRS-1 droplet. Images acquired every 1 minute, movie presented at 10 frames per second. Scale bar: 10 μm. (MOV 6,458 kb)

Supplementary Movie 7. LD dynamics
Oleic acid-treated HeLa cells were imaged by time-lapse ExAPC microscopy to visualize LD dynamics. Images acquired every 20 seconds, movie presented at 10 frames per second. Scale bar: 1 μm. (MOV 64,065 kb)

Supplementary Movie 8. Mitochondria fission
Hep3B cells were imaged by time-lapse ExAPC microscopy to visualize mitochondria fission. Images acquired every 1 second, movie presented at 10 frames per second. Scale bar: 1 μm. (MOV 11,651 kb)

Supplementary Movie 9. Mitochondria fusion (end-to-end)
Hep3B cells were imaged by time-lapse ExAPC microscopy to visualize end-to-end fusion of mitochondria. Images acquired every 1 second, movie presented at 10 frames per second. Scale bar: 1 μm. (MOV 43,219 kb)

Supplementary Movie 10. Mitochondria fusion (end-to-side)
Hep3B cells were imaged by time-lapse ExAPC microscopy to visualize end-to-side fusion of mitochondria. Images acquired every 1 second, movie presented at 10 frames per second. Scale bar: 1 μm. (MOV 32,757 kb)

Supplementary Movie 11. FCCP treatment-induced changes in mitochondrial morphology in Hep3B cells
Hep3B cells were imaged by time-lapse ExAPC microscopy to visualize morphological changes of

mitochondria in the presence of FCCP. Hep3B cells were treated with 40 μM FCCP at frame 301. Images acquired every 1 second, movie presented at 10 frames per second. Scale bar: 1 μm. (MOV 107,116 kb)

Supplementary Movie 12. FCCP treatment-induced changes in mitochondrial morphology in U-2 OS cells

U-2 OS cells were imaged by time-lapse ExAPC microscopy to visualize morphological changes of mitochondria in the presence of FCCP. U-2 OS cells were treated with 40 μM FCCP at frame 301. Images acquired every 1 second, movie presented at 10 frames per second. Scale bar: 1 μm. (MOV 69,553 kb)

References

1. Rafelski, S.M. & Marshall, W.F. Building the cell: design principles of cellular architecture. *Nat Rev Mol Cell Biol* **9**, 593-602 (2008).
2. Perkins, H.T. & Allan, V. Intertwined and finely balanced: endoplasmic reticulum morphology, dynamics, function, and diseases. *Cells* **10** (2021).
3. Liu, J. et al. The role of the golgi apparatus in disease (review). *Int J Mol Med* **47**(2021).
4. Heckenbach, I. et al. Nuclear morphology is a deep learning biomarker of cellular senescence. *Nat. Aging* **2**, 742-755 (2022).
5. Chen, W., Zhao, H. & Li, Y. Mitochondrial dynamics in health and disease: mechanisms and potential targets. *Signal Transduct Target Ther* **8**, 333 (2023).
6. Hickey, S.M. et al. Fluorescence microscopy-an outline of hardware, biological handling, and fluorophore considerations. *Cells* **11** (2021).
7. Viana, M.P. et al. Integrated intracellular organization and its variations in human iPS cells. *Nature* **613**, 345-354 (2023).
8. Kiepas, A., Voorand, E., Mubaid, F., Siegel, P.M. & Brown, C.M. Optimizing live-cell fluorescence imaging conditions to minimize phototoxicity. *J Cell Sci* **133** (2020).
9. Strack, R. Imaging without the labels. *Nat. Methods* **19**, 30 (2022).
10. Sandoz, P.A., Tremblay, C., van der Goot, F.G. & Frechin, M. Image-based analysis of living mammalian cells using label-free 3D refractive index maps reveals new organelle dynamics and dry mass flux. *PLoS Biol* **17**, e3000553 (2019).
11. Guo, S., Ma, Y., Pan, Y., Smith, Z.J. & Chu, K. Organelle-specific phase contrast microscopy enables gentle monitoring and analysis of mitochondrial network dynamics. *Biomed Opt Express* **12**, 4363-4379 (2021).
12. Zhang, C. & Boppart, S.A. Tracking the formation and degradation of fatty-acid-accumulated mitochondria using label-free chemical imaging. *Sci Rep* **11**, 6671 (2021).
13. Pelc, R., Hostounský, Z., Otaki, T. & Katoh, K. Conventional, apodized, and relief phase-contrast microscopy. In: Pelc, R., Walz, W., Doucette, J.R. (eds) Neurohistology and Imaging Techniques. *Neuromethods* **153** (2020).
14. Pelc, R., Hostounsky, Z. & Otaki, T. Correlation between off-axis illumination and apodized phase-contrast: two complementary microscopic phase-imaging modes. *J Biomed Opt* **13**, 054067 (2008).
15. Ma, Y. et al. Label-free imaging of intracellular organelle dynamics using flat-fielding quantitative phase contrast microscopy (FF-QPCM). *Opt Express* **30**, 9505-9520 (2022).
16. Duster, R., Kaltheuner, I.H., Schmitz, M. & Geyer, M. 1,6-Hexanediol, commonly used to dissolve liquid-liquid phase separated condensates, directly impairs kinase and phosphatase activities. *J Biol Chem* **296**, 100260 (2021).

17. Gao, C. et al. Hyperosmotic-stress-induced liquid-liquid phase separation of ALS-related proteins in the nucleus. *Cell Rep* **40**, 111086 (2022).
18. Lafontaine, D.L.J., Riback, J.A., Bascetin, R. & Brangwynne, C.P. The nucleolus as a multiphase liquid condensate. *Nat Rev Mol Cell Biol* **22**, 165-182 (2021).
19. Boucher, J., Kleinridders, A. & Kahn, C.R. Insulin receptor signaling in normal and insulin-resistant states. *Cold Spring Harb Perspect Biol* **6** (2014).
20. Takahashi, S.I. IGF research 2016-2018. *Growth Horm IGF Res* **48-49**, 65-69 (2019).
21. Hakuno, F. et al. The novel functions of high-molecular-mass complexes containing insulin receptor substrates in mediation and modulation of insulin-like activities: emerging concept of diverse functions by IRS-associated proteins. *Front Endocrinol (Lausanne)* **6**, 73 (2015).
22. Gao, X.K. et al. Phase separation of insulin receptor substrate 1 drives the formation of insulin/IGF-1 signalosomes. *Cell Discov* **8**, 60 (2022).
23. Gao, X.K. et al. VAPB-mediated ER-targeting stabilizes IRS-1 signalosomes to regulate insulin/IGF signaling. *Cell Discov* **9**, 83 (2023).
24. Khandelia, H., Duelund, L., Pakkanen, K.I. & Ipsen, J.H. Triglyceride blisters in lipid bilayers: implications for lipid droplet biogenesis and the mobile lipid signal in cancer cell membranes. *PLoS One* **5**, e12811 (2010).
25. Choudhary, V., Ojha, N., Golden, A. & Prinz, W.A. A conserved family of proteins facilitates nascent lipid droplet budding from the ER. *J Cell Biol* **211**, 261-71 (2015).
26. Wilfling, F. et al. Triacylglycerol synthesis enzymes mediate lipid droplet growth by relocalizing from the ER to lipid droplets. *Dev Cell* **24**, 384-99 (2013).
27. Gao, G. et al. Control of lipid droplet fusion and growth by CIDE family proteins. *Biochim Biophys Acta Mol Cell Biol Lipids* **1862**, 1197-1204 (2017).
28. Tatenaka, Y. et al. Monitoring lipid droplet dynamics in living cells by using fluorescent probes. *Biochemistry* **58**, 499-503 (2019).
29. Kassan, A. et al. Acyl-CoA synthetase 3 promotes lipid droplet biogenesis in ER microdomains. *J Cell Biol* **203**, 985-1001 (2013).
30. Gao, Q. & Goodman, J.M. The lipid droplet-a well-connected organelle. *Front Cell Dev Biol* **3**, 49 (2015).
31. Tabara, L.C., Morris, J.L. & Prudent, J. The complex dance of organelles during mitochondrial division. *Trends Cell Biol* **31**, 241-253 (2021).
32. Archer, S.L. Mitochondrial dynamics--mitochondrial fission and fusion in human diseases. *N Engl J Med* **369**, 2236-51 (2013).
33. Harwig, M.C. et al. Methods for imaging mammalian mitochondrial morphology: A prospective on MitoGraph. *Anal Biochem* **552**, 81-99 (2018).
34. Kleele, T. et al. Distinct fission signatures predict mitochondrial degradation or biogenesis. *Nature*

593, 435-439 (2021).

35. Sebastian, D., Palacin, M. & Zorzano, A. Mitochondrial dynamics: coupling mitochondrial fitness with healthy aging. *Trends Mol Med* **23**, 201-215 (2017).
36. Chiu, Y.H., Lin, S.A., Kuo, C.H. & Li, C.J. Molecular machinery and pathophysiology of mitochondrial dynamics. *Front Cell Dev Biol* **9**, 743892 (2021).
37. Gao, S. & Hu, J. Mitochondrial Fusion: The machineries in and out. *Trends Cell Biol* **31**, 62-74 (2021).
38. Liu, X., Weaver, D., Shirihai, O. & Hajnoczky, G. Mitochondrial 'kiss-and-run': interplay between mitochondrial motility and fusion-fission dynamics. *EMBO J* **28**, 3074-89 (2009).
39. Frank, S. et al. The role of dynamin-related protein 1, a mediator of mitochondrial fission, in apoptosis. *Dev Cell* **1**, 515-25 (2001).
40. Huang, X. et al. Kissing and nanotunneling mediate intermitochondrial communication in the heart. *Proc Natl Acad Sci U S A* **110**, 2846-51 (2013).
41. Hirano, M. et al. A highly photostable and bright green fluorescent protein. *Nat Biotechnol* **40**, 1132-1142 (2022).
42. Ando, R. et al. StayGold variants for molecular fusion and membrane-targeting applications. *Nat Methods* (2023).
43. Banani, S.F., Lee, H.O., Hyman, A.A. & Rosen, M.K. Biomolecular condensates: organizers of cellular biochemistry. *Nat Rev Mol Cell Biol* **18**, 285-298 (2017).
44. Alberti, S., Gladfelter, A. & Mittag, T. Considerations and challenges in studying liquid-liquid phase separation and biomolecular condensates. *Cell* **176**, 419-434 (2019).
45. Alberti, S. & Dormann, D. Liquid-liquid phase separation in disease. *Annu Rev Genet* **53**, 171-194 (2019).
46. Alberti, S. & Hyman, A.A. Biomolecular condensates at the nexus of cellular stress, protein aggregation disease and ageing. *Nat Rev Mol Cell Biol* **22**, 196-213 (2021).
47. Mitrea, D.M., Mittasch, M., Gomes, B.F., Klein, I.A. & Murcko, M.A. Modulating biomolecular condensates: a novel approach to drug discovery. *Nat Rev Drug Discov* **21**, 841-862 (2022).
48. Miura, S. et al. Functional conservation for lipid storage droplet association among Perilipin, ADRP, and TIP47 (PAT)-related proteins in mammals, Drosophila, and Dictyostelium. *J Biol Chem* **277**, 32253-7 (2002).
49. Olzmann, J.A. & Carvalho, P. Dynamics and functions of lipid droplets. *Nat Rev Mol Cell Biol* **20**, 137-155 (2019).
50. Gong, J. et al. Fsp27 promotes lipid droplet growth by lipid exchange and transfer at lipid droplet contact sites. *J Cell Biol* **195**, 953-63 (2011).
51. Ponten, F., Jirstrom, K. & Uhlen, M. The Human Protein Atlas--a tool for pathology. *J Pathol* **216**, 387-93 (2008).

52. Karlsson, M. et al. A single-cell type transcriptomics map of human tissues. *Sci Adv* **7** (2021).
53. Wang, H. et al. Seipin is required for converting nascent to mature lipid droplets. *Elife* **5** (2016).
54. Tilokani, L., Nagashima, S., Paupe, V. & Prudent, J. Mitochondrial dynamics: overview of molecular mechanisms. *Essays Biochem* **62**, 341-360 (2018).
55. Miyamoto, T. et al. Rapid manipulation of mitochondrial morphology in a living cell with iCMM. *Cell Rep Methods* **1**, 100052 (2021).
56. Archer, S.L. Mitochondrial fission and fusion in human diseases. *N Engl J Med* **370**, 1074 (2014).
57. Navaratnarajah, T., Anand, R., Reichert, A.S. & Distelmaier, F. The relevance of mitochondrial morphology for human disease. *Int J Biochem Cell Biol* **134**, 105951 (2021).
58. Wada, T. et al. Single-cell information analysis reveals that skeletal muscles incorporate cell-to-cell variability as information not noise. *Cell Rep* **32**, 108051 (2020).
59. Baysoy, A., Bai, Z., Satija, R. & Fan, R. The technological landscape and applications of single-cell multi-omics. *Nat Rev Mol Cell Biol* **24**, 695-713 (2023).
60. Kobayashi-Kirschvink, K.J. et al. Linear Regression Links Transcriptomic Data and Cellular Raman Spectra. *Cell Syst* **7**, 104-117 e4 (2018).
61. Kobayashi-Kirschvink, K.J. et al. Prediction of single-cell RNA expression profiles in live cells by Raman microscopy with Raman2RNA. *Nat Biotechnol* (2024).
62. Nishimura, T. et al. Generation of rejuvenated antigen-specific T cells by reprogramming to pluripotency and redifferentiation. *Cell Stem Cell* **12**, 114-26 (2013).
63. Nakagawa, M. et al. A novel efficient feeder-free culture system for the derivation of human induced pluripotent stem cells. *Sci Rep* **4**, 3594 (2014).

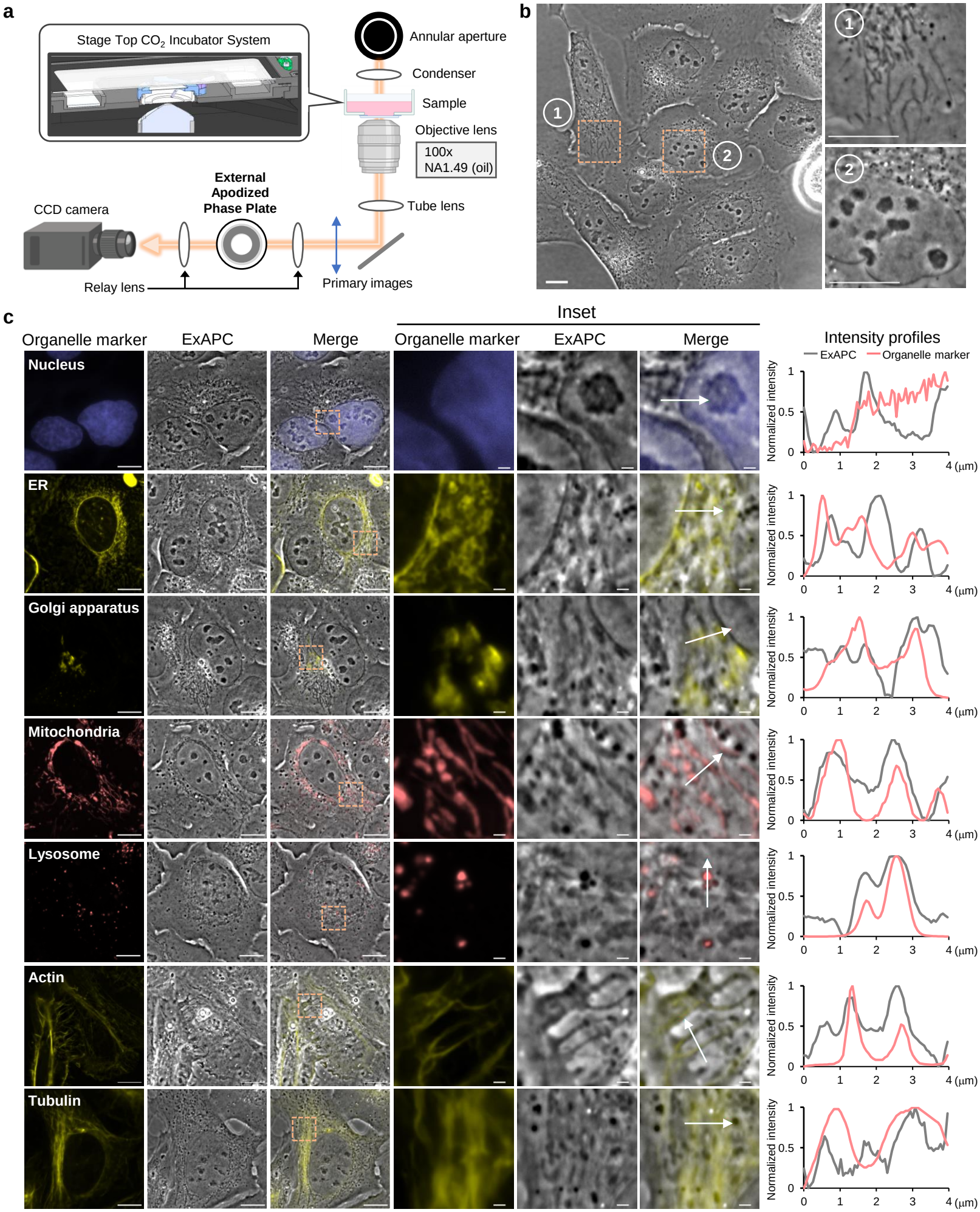

Figure 1. Sari et al.

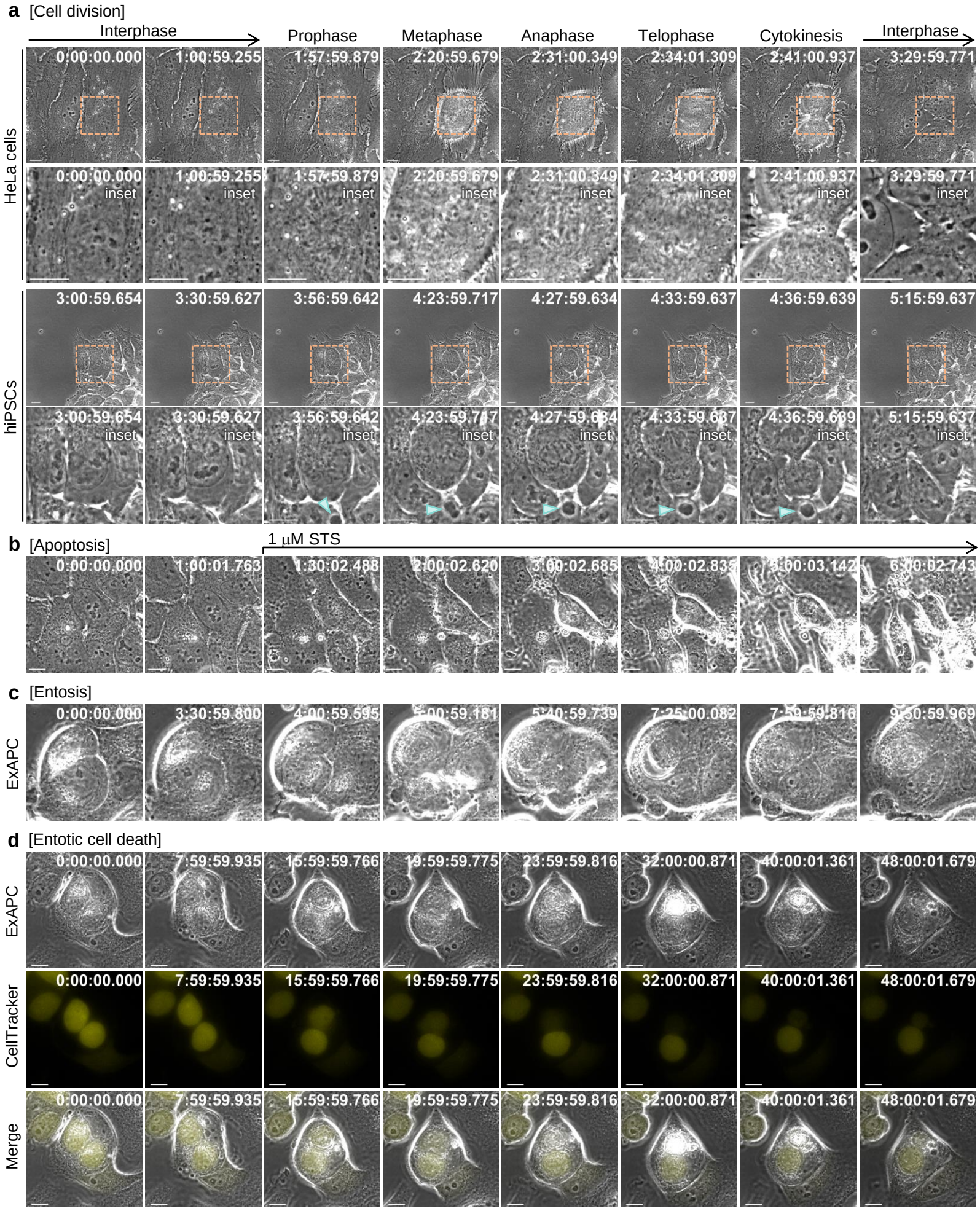

Figure 2. Sari et al.

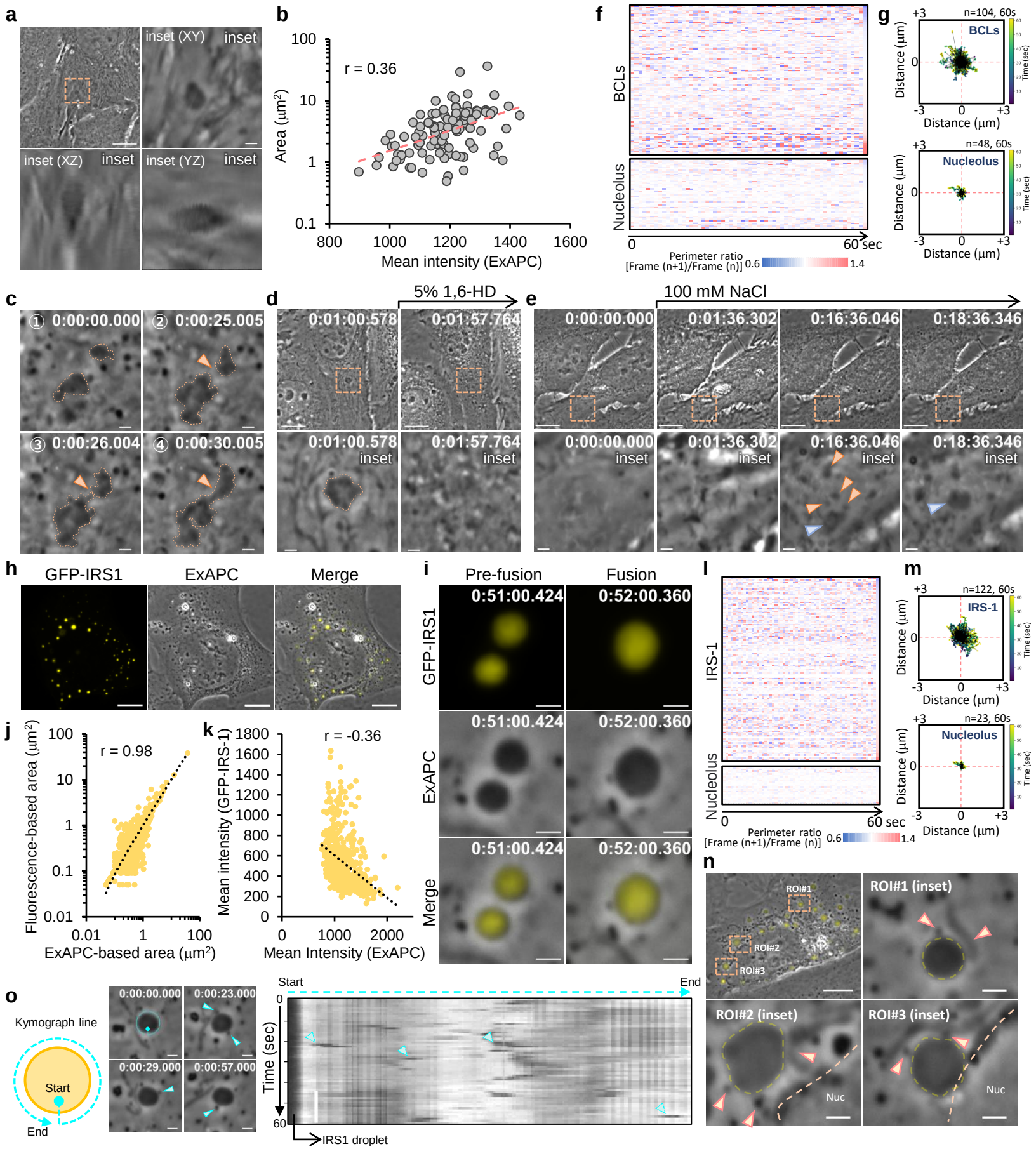

Figure 3. Sari et al.

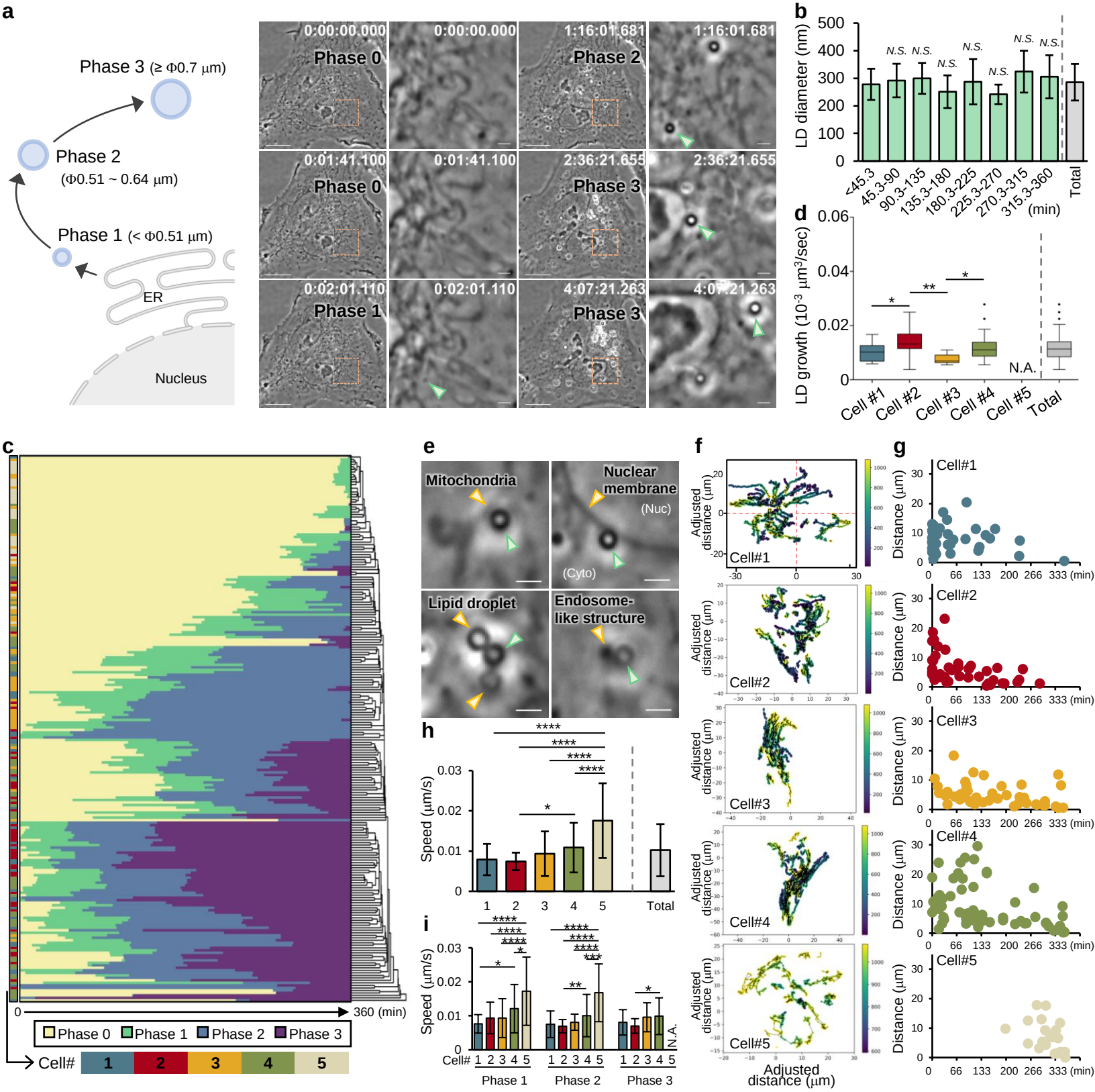

Figure 4. Sari et al.

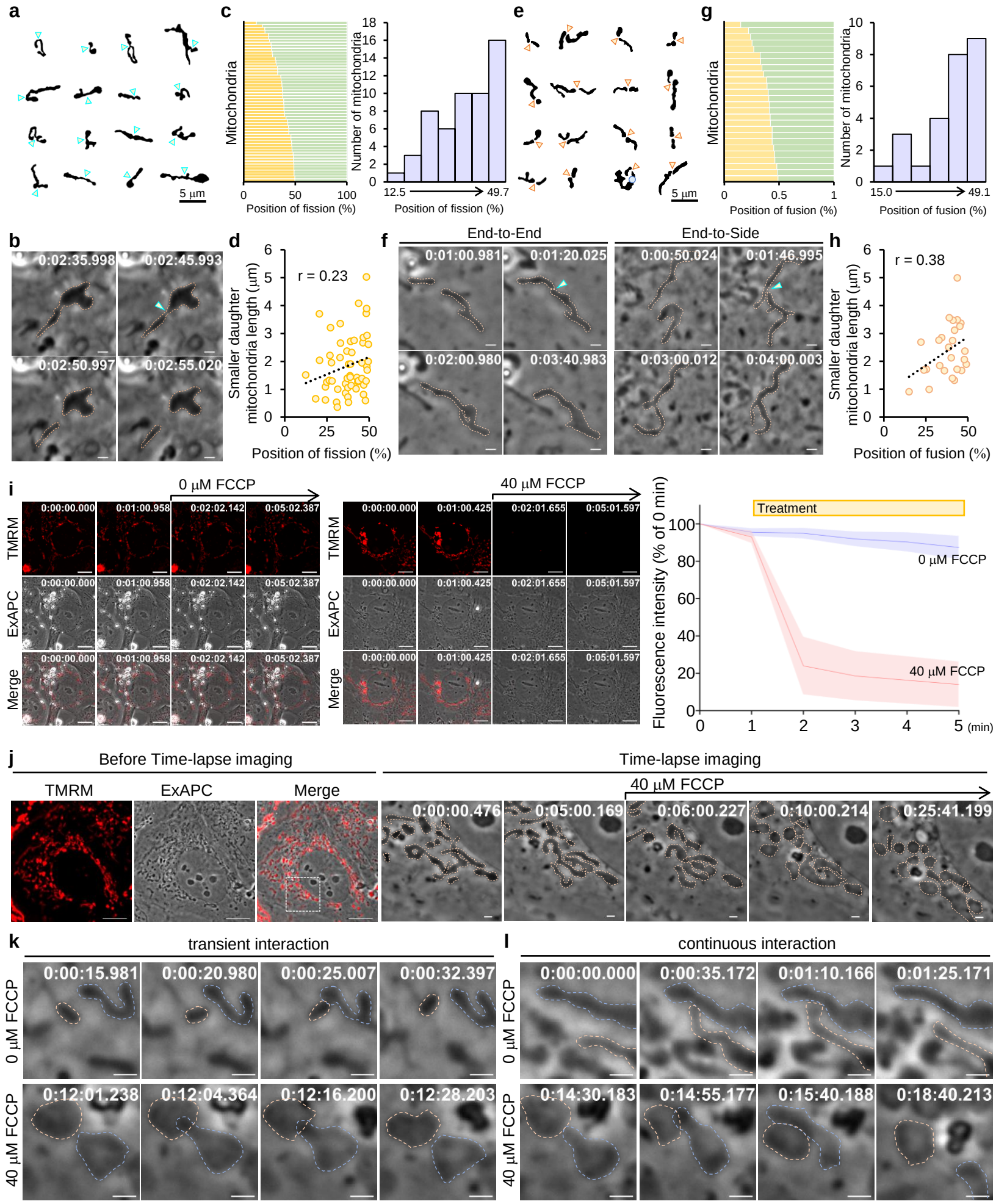

Figure 5. Sari et al.

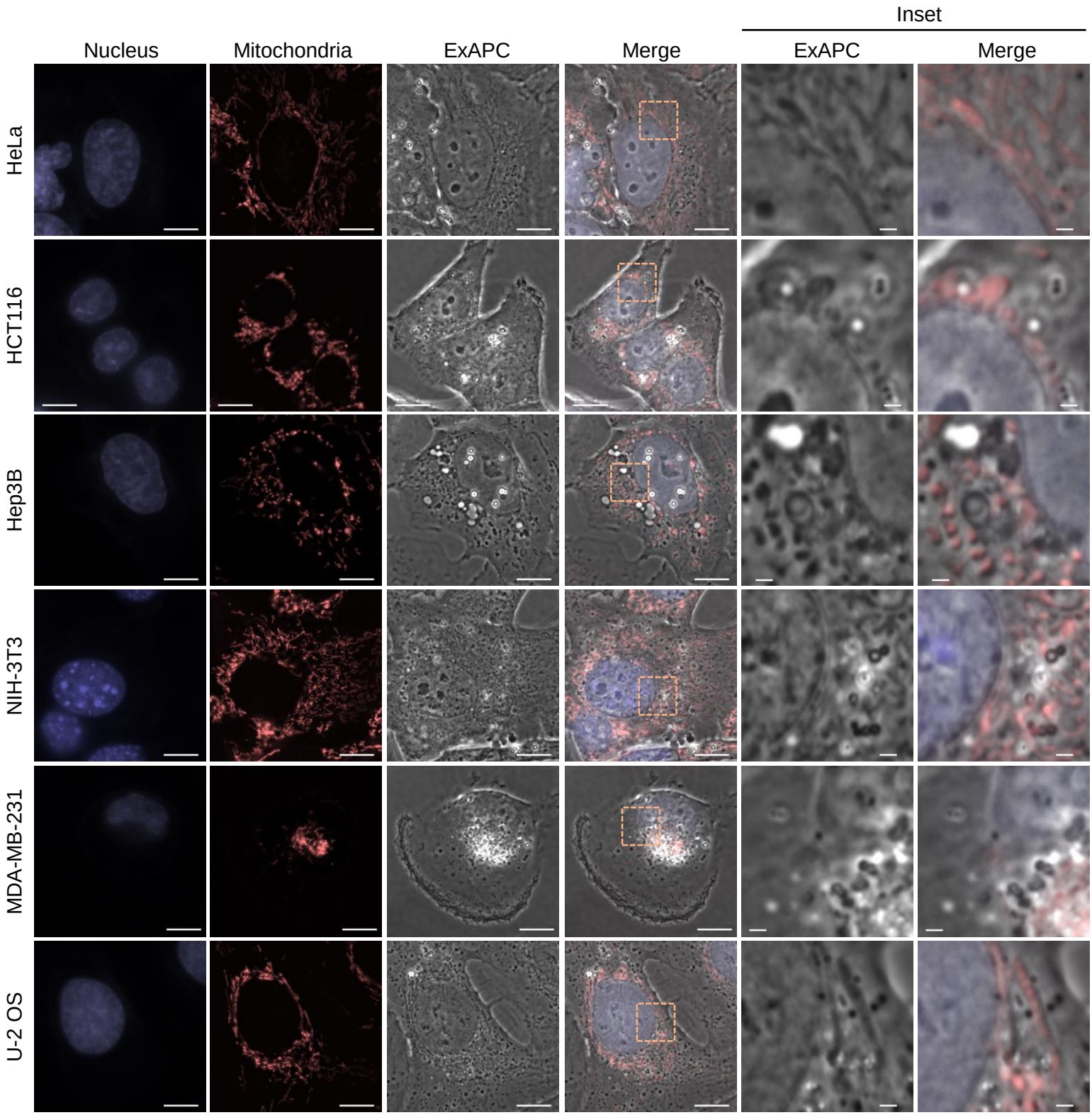

Supplementary Figure 1. Sari et al.

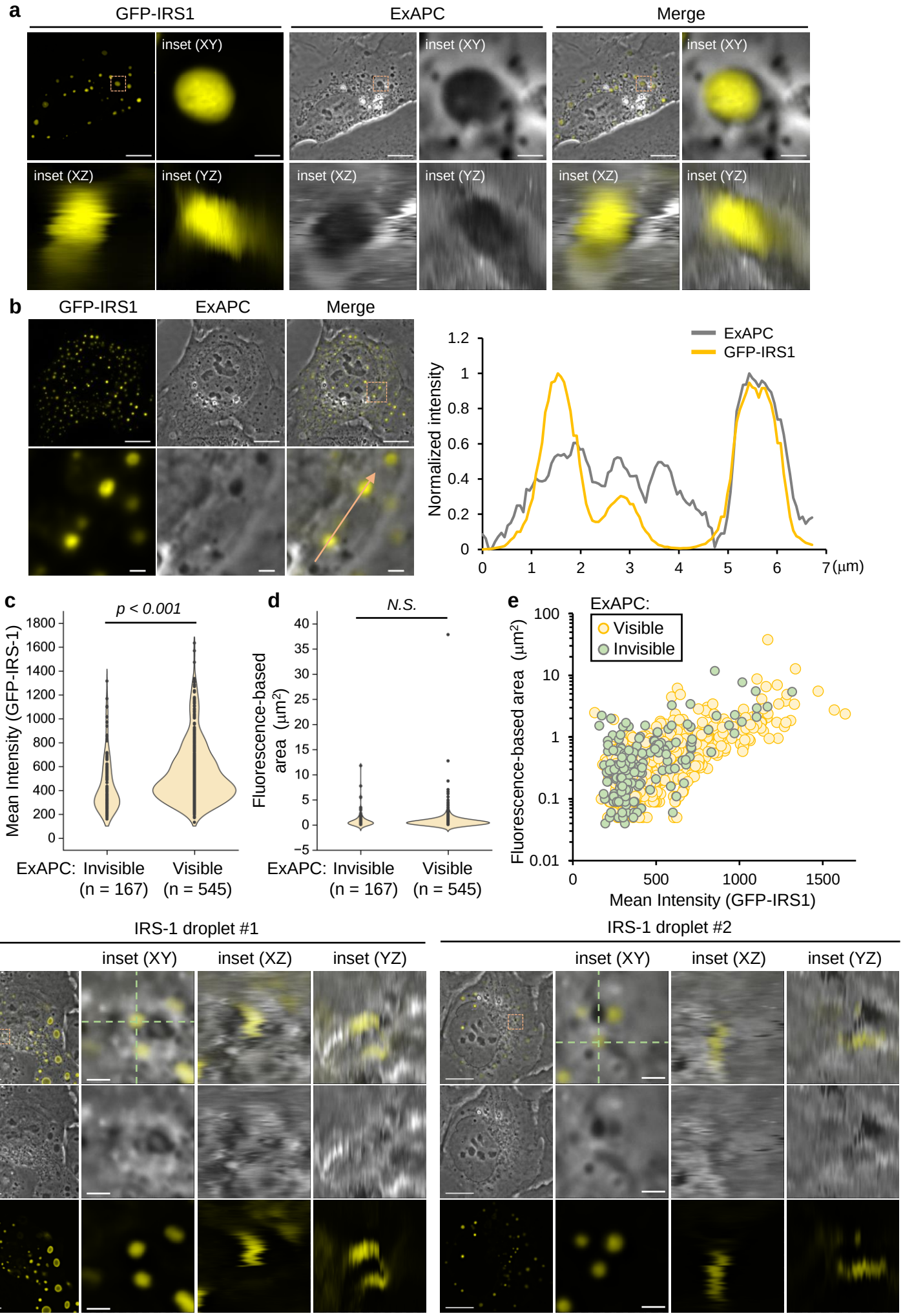

Supplementary Figure 2. Sari et al.

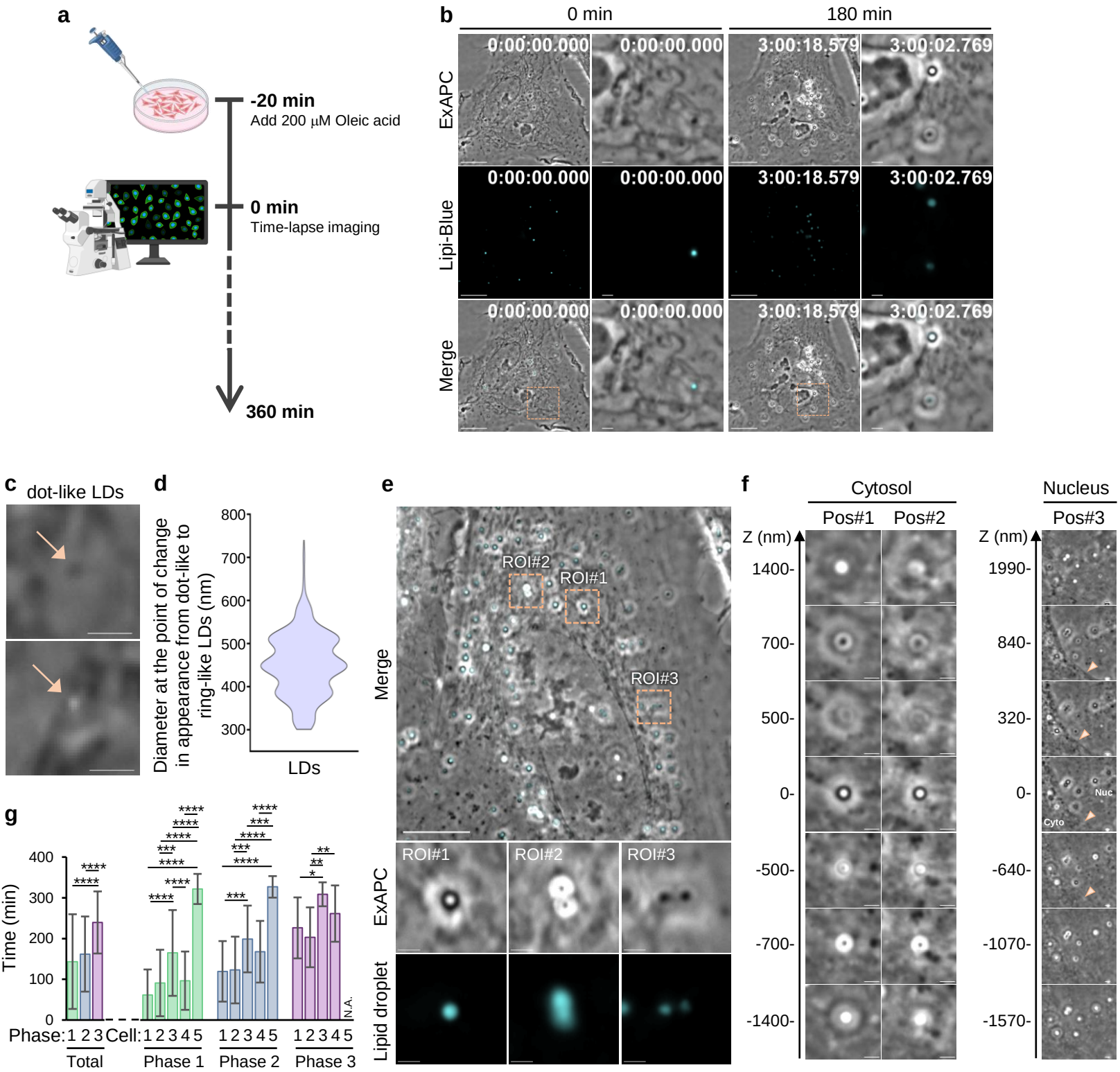

Supplementary Figure 3. Sari et al.

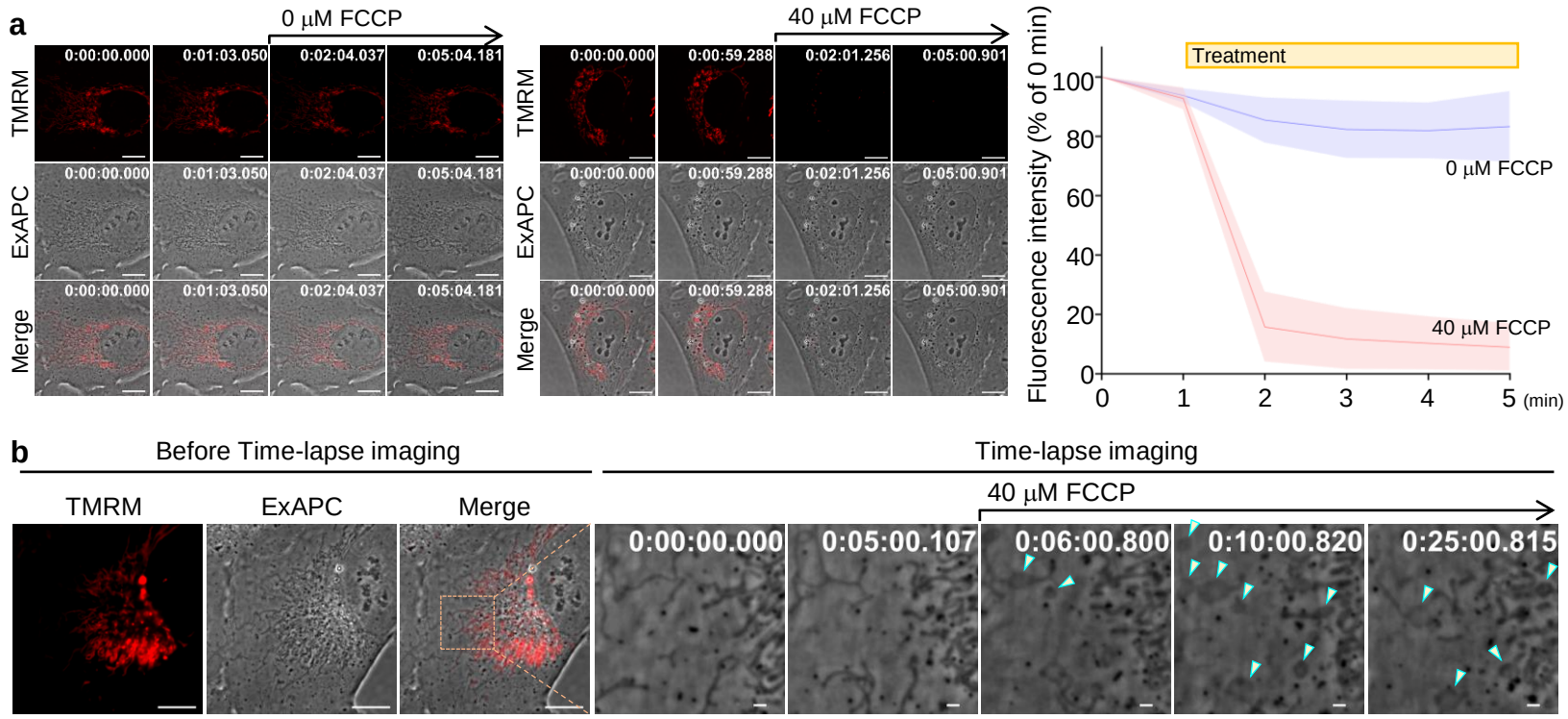

Supplementary Figure 4. Sari et al.